Improved simulation of the polar atmospheric boundary layer by accounting for aerodynamic roughness in the parameterisation of surface scalar exchange over sea ice

A. D. Elvidge[1], I. A. Renfrew[1], J. M. Edwards[2], I. M. Brooks[3], P. Srivastava[3,4], A. I. Weiss[5]

[1]School of Environmental Sciences, University of East Anglia, Norwich, United Kingdom

[2]The Met Office, Exeter, United Kingdom

[3]School of Earth and Environment, University of Leeds, Leeds, United Kingdom

[4]Centre of Excellence in Disaster Mitigation and Management, Indian Institute of Technology Roorkee, Roorkee, Uttarakhand, India

[5]British Antarctic Survey, Cambridge, United Kingdom

Journal of Advances in Modeling Earth Systems

Submitted on: 14 July 2022

Abstract

A new, simple parameterisation scheme for scalar (heat and moisture) exchange over sea ice and the marginal ice zone is tested in a numerical weather and climate prediction model. This new "*Blended A87*" scheme accounts for the influence of aerodynamic roughness on the relationship between momentum and scalar exchange over consolidated sea ice, in line with long-standing theory and recent field observations, and in contrast to the crude schemes currently operational in most models. Using aircraft observations and Met Office Unified Model simulations of cold-air outbreak (CAO) conditions over aerodynamically rough sea ice, we demonstrate striking improvements in model performance when the *Blended A87* scheme replaces the model's operational treatment for surface scalar exchange, provided that the aerodynamic roughness over consolidated ice is appropriately prescribed. The mean biases in surface sensible heat flux, surface latent heat flux, near-surface air temperature and surface temperature reduce from 25 to 11 W m^{-2}, 22 to 12 W m^{-2}, 0.8 to 0.0 K, and 1.4 to 0.8 K, respectively. We demonstrate that such impacts on surface exchange over sea ice can have a marked impact on the evolution of the atmospheric boundary layer across hundreds of kilometres downwind of the sea ice during CAO conditions in the model. Our results highlight the importance of spatiotemporal variability in the topography of consolidated sea ice for both momentum and scalar exchange over sea ice; accounting for which remains a challenge for modelling polar weather and climate.

Plain Language Summary

A new algorithm for the turbulent exchange of scalar quantities (specifically heat and moisture) between the atmosphere and the ice-covered oceans of the polar regions is tested in a state-of-the-art weather and climate model. The algorithm is applicable both over consolidated sea ice and in regions characterised by a mixture of open seawater and ice. It accounts for the influence of aerodynamic roughness (a function of wind speed and the fine-scale topographic roughness of the surface), in line with long-standing theory and recent field observations, and in contrast to the crude schemes currently operational in most models. Using low-altitude aircraft observations obtained from over the Arctic Ocean,

we demonstrate striking improvements in model performance when the new algorithm replaces the model's operational treatment for surface scalar exchange, provided that the aerodynamic roughness over consolidated ice is appropriately prescribed. The mean biases in surface sensible heat flux, surface latent heat flux, near-surface air temperature and surface temperature reduce from 25 to 11 W m^{-2}, 22 to 12 W m^{-2}, 0.8 to 0.0 K, and 1.4 to 0.8 K, respectively. We demonstrate that such impacts on surface exchange over sea ice can have a significant impact on model prediction of high-latitude weather.

Key points

- Numerical model reproduction of scalar fluxes over sea ice is improved with a new parameterisation that accounts for aerodynamic roughness
- The properties and structure of the polar atmospheric boundary layer are sensitive to the implementation of this new parameterisation
- The benefit of the parameterization accounting for aerodynamic roughness hinges on the appropriate prescription of sea-ice topography

Keywords:
surface exchange parameterization
turbulent fluxes
sea ice
air-sea-ice interaction
atmospheric boundary layer
polar climate

1 | Introduction

Rapid climatic change in the polar regions presents significant socioeconomic threats and opportunities, demanding improved predictions of polar weather and climate across a range of spatial and temporal scales (e.g., Jung et al. 2016; Sigmond et al., 2018; Overland et al., 2019). One important component of the polar climate system in which there remains considerable uncertainty is the turbulent exchange of physical and chemical constituents between the atmosphere and the ocean in the vicinity of sea ice. Such exchange plays an

important role in the weather and climate of the mid- to high-latitudes (e.g., Rae et al., 2014; Young et al., 2016; Renfrew et al., 2019a; Pope et al., 2020); in ocean circulation and deep water formation (e.g., Renfrew et al., 2019b, 2021; Stössel et al., 2008); and in the extent and transport of sea ice (e.g., Fichefet and Maqueda, 1997; Tsamados et al., 2014; Vavrus and Harrison, 2003; Vihma et al., 2009; Raphael, 2007). It is therefore vital that this exchange – notably of momentum, heat and moisture – is accurately represented in numerical models of the atmosphere, ocean and sea ice via appropriate subgrid-scale surface exchange parameterisation schemes.

Surface exchange schemes provide estimates of surface fluxes – for example, for momentum, τ; sensible heat, SH; and moisture (or latent heat), LH; – over a given surface type as follows:

$$\tau_k = \rho\, C_{DNk}\, U^2, \tag{1}$$

$$SH_k = c_p\, \rho\, C_{HNk}\, U\, (\theta_s - \theta), \tag{2}$$

$$LH_k = L_V\, \rho\, C_{ENk}\, U\, (q_s - q), \tag{3}$$

where subscript k is the surface type, either ice (subscript i) or seawater (subscript w); U is wind speed; $\theta_s - \theta$ and $q_s - q$ are the surface-air differences in potential temperature and specific humidity, respectively; ρ is the air density; c_p is the specific heat capacity of air; L_V is the latent heat of vaporization; and C_{DN}, C_{HN} and C_{EN} are the exchange coefficients for momentum, heat and moisture, respectively. For a given surface type, the surface exchange coefficients (adjusted for a neutral stratified surface layer) are related to the surface roughness lengths for momentum (z_0), heat (z_{0T}) and moisture (z_{0q}) using Monin-Obukhov similarity theory (Monin and Obukhov, 1954) as follows:

$$C_{DNk} = \frac{\kappa^2}{\ln(z/z_{0k})^2}, \tag{4}$$

$$C_{HNk} = \frac{\kappa^2}{\ln(z/z_{0k})\, \ln(z/z_{0Tk})}, \tag{5}$$

$$C_{ENk} = \frac{\kappa^2}{\ln(z/z_{0k})\,\ln(z/z_{0qk})}, \quad (6)$$

where κ is the von Kármán constant (0.4); z is the reference height at which the exchange coefficients are evaluated (here 10 m, as is standard).

The surface roughness lengths must be obtained empirically. However, obtaining the necessary in-situ measurements in the polar regions is challenging, and this has limited our capacity to constrain surface exchange schemes for sea ice. In recent years, substantial progress has been made with significant new data sets and analyses available (e.g., Elvidge et al. 2016; Elvidge et al. 2021; Srivastava et al. 2022).

A parameterisation framework for momentum exchange over sea ice and the marginal ice zone (MIZ) has been established that accounts independently for *skin drag* associated with friction in the viscous sublayer and *form drag* associated with flow separation and pressure differentials generated by airflow over the vertical edges of ice floes in the MIZ (Arya, 1973, 1975; Birnbaum and Lüpkes, 2002; Garbrecht et al., 2002; Lüpkes et al., 2012; Lüpkes and Gryanik, 2015). Here, C_{DN} and τ over ice (C_{DNi} and τ_i) are derived using equations (1) and (4), then τ is given as a function of sea-ice concentration using the so-called mosaic or flux averaging approach (e.g. Claussen, 1990; Vihma, 1995) as follows:

$$\tau = (1 - A)\,\tau_w + A\,\tau_i + \tau_f, \quad (7)$$

where τ_w is the momentum flux (or drag) over seawater (obtained from an ocean surface exchange scheme) and τ_f is the form drag from ice floe edges (obtained following, for example, Lüpkes et al., 2012, and Elvidge et al., 2016, in the case of the Met Office Unified Model, MetUM). Schemes using this framework have been evaluated and constrained using in-situ aircraft, tower and ship observations (e.g. Lüpkes & Birnbaum, 2005; Elvidge et al., 2016, 2021; Srivastava et al., 2022) and implemented in a range of numerical models, including the MetUM (Renfrew et al., 2019a), the European Centre for Medium-Range Weather Forecasts Integrated Forecast System (IFS) (Roberts et al., 2018), the Los Alamos Sea Ice Model (CICE) (Tsamados et al., 2014), and a regional coupled climate model (HIRHAM–NAOSIM 2.0) (Yu et al., 2020).

A major remaining deficiency of even the most sophisticated surface exchange schemes for sea ice is in the representation of z_0 over consolidated sea ice (i.e., z_{0i}). This important parameter is known to vary by several orders of maginitude in space and time due to variability in sea-ice topography related to characteristics such as sea-ice type, age and thickness; the presence of pressure ridging; and hydrological systems (e.g. Castellani et al., 2014; Elvidge et al., 2016; Petty et al., 2017; Srivastava et al., 2022). However, there is as yet no reliable recognised method by which to represent this z_{0i} variability in numerical models. Consequently, z_{0i} is currently set as a fixed value in most models; for example 5×10^{-4} and 1×10^{-3} m in the MetUM and IFS, respectively. Note that z_{0i} appears in the derivation of both the momentum and scalar exchange coefficients (see equations 4-6), so this deficiency affects the parameterization of both momentum and scalar fluxes over sea ice.

The parameterisation of scalar exchanges over sea ice and the MIZ has received less attention than that of momentum exchange, and the representation of heat and moisture fluxes over sea ice in numerical models remains crude. In the MetUM – the numerical weather prediction (NWP) model used in this study – over sea ice z_{0T} and z_{0q} are proportional to z_0 and given by $z_{0Ti} = z_{0qi} = 0.2\ z_{0i}$ (as depicted in Figure 1). Then C_{HNi} and C_{ENi} and the associated fluxes (SH_i and LH_i) are derived using equations (2), (3), (5) and (6). As with τ, SH and LH over sea ice and the MIZ are then derived using the mosaic approach:

$$SH = (1 - A)\ SH_w + A\ SH_i\ , \tag{8}$$

$$LH = (1 - A)\ LH_w + A\ LH_i\ , \tag{9}$$

where A is sea-ice concentration, and SH_w and LH_w are the sensible and latent heat fluxes over seawater (again obtained from an ocean surface exchange scheme). Similar treatments are found in other state-of-the-art numerical models including the IFS and CICE. Note that, in contrast to momentum exchange, the effect of ice floe edges on scalar exchange is currently unaccounted for in operational NWP models. Lüpkes and Gryanik (2015) suggest a framework for incorporating this effect.

It is well established in the literature (e.g., Andreas, 1987) that surface scalar exchange over ice is dependent on aerodynamic roughness, expressed as the roughness Reynolds number over ice, R_{*i}:

$$R_{*i} = \frac{z_{0i}\, u_{*i}}{\nu}, \tag{10}$$

where ν is kinematic viscosity; u_{*i} is friction velocity over ice given by:

$$u_{*i} = \frac{\kappa\, U}{\ln(z/z_{0i}) - \varphi}; \tag{11}$$

where φ is a stability correction function (see for example Stull, 1988). A lack of sensitivity to R_{*i} in the representation of surface scalar exchange has recently been highlighted as a major deficiency of existing surface exchange parameterization schemes for sea ice (Elvidge et al., 2021; hereafter E21). E21 used in-situ aircraft observations and offline parameterization experiments to demonstrate for the first time that whilst these existing schemes can – with appropriate tuning of z_{0i} – perform well for the MIZ in an aerodynamically *smooth* sea ice regime (defined by Roughness Reynolds Number, R_{*i} < 0.135), they are inappropriate and perform poorly in an aerodynamically *rough* regime (R_{*i} ≥ 2.5). This is because in a *rough* regime, the introduction of pressure forces (form drag) across surface roughness elements extending above the viscous sublayer violates the assumption that momentum and heat transfer depend on the same turbulent eddies. Consequently, z_{0Ti} and z_{0qi} cannot be proportional to z_{0i}. Instead, $\frac{z_{0Ti}}{z_{0i}}$ and $\frac{z_{0qi}}{z_{0i}}$ are inversely correlated to aerodynamic roughness in *rough* conditions.

A more sophisticated theoretical model for surface heat and moisture exchange over sea ice was developed by Andreas (1987). Based on surface-renewal theory, it provides $\frac{z_{0Ti}}{z_{0i}}$ and $\frac{z_{0qi}}{z_{0i}}$ as non-linear functions of R_{*i} (see Figure 1). This "A87 theoretical model" applies distinct, physically justified treatments for scalar exchange under *smooth* conditions (an advection-diffusion model) and *rough* conditions (a diffusion model). It has been shown to skillfully reproduce observed surface scalar fluxes over consolidated ice and snow surfaces, e.g. over sea ice (Andreas, 1987; Andreas et al., 2010; E21) and over mountain glaciers

(Fitzpatrick et al., 2019). However, it is only appropriate over consolidated ice and, consequently, not over the heterogenous ice-water mix of the MIZ.

To tackle the MIZ and other areas of unconsolidated sea ice, E21 proposed a new parameterization framework that blends the A87 scheme with the output of an ocean surface exchange scheme. Here, $\frac{z_{0Ti}}{z_{0i}}$ and $\frac{z_{0qi}}{z_{0i}}$ are derived from R_{*i} using polynomial approximations of the A87 theory (see equation (53) and Table I in Andreas, 1987). The scalar exchange coefficients and fluxes for consolidated sea ice area then derived using equations (2), (3), (5) and (6), and fluxes across the MIZ are determined using the same mosaic approach as in the operational MetUM scheme (equations 8 and 9). In offline tests, this *Blended A87* scheme performed much better than the crude operational schemes in the MetUM and IFS for the aerodynamically rough conditions documented in observations obtained during the field campaign of the Iceland Greenland Seas Project (IGP) (E21).

In this paper, we use MetUM sensitivity experiments in tandem with aircraft observations obtained from two Arctic field campaigns, to establish:

- the impact of the *Blended A87* scheme on the reproduction of surface heat and moisture fluxes over sea ice in an NWP model;
- the sensitivity of Arctic boundary-layer conditions to changes in surface heat and moisture fluxes over sea ice in an NWP model;
- the broader implications and current limitations of introducing aerodynamic-roughness dependence to surface scalar exchange over sea ice.

2 | Methods

2.1 | Atmospheric modelling

The MetUM is a state-of-the-art atmospheric model solving the deep non-hydrostatic compressible equations for a fluid and incorporating parametrisations for physical processes including radiation, microphysics, orographic drag, boundary-layer turbulence and surface exchange. It is used by the Met Office for their operational weather forecasting and as a component in all their climate models (e.g. Walters et al., 2019). Here we employ regional simulations in the MetUM, with model physics based on the Regional

Atmosphere and Land Science Configuration 1 for Mid-Latitudes (RAL1-M; Bush et al., 2020). The regional domain used here covers the northern Iceland Sea and southwest Greenland Sea (see Figure 2) and uses a horizontal grid spacing of 2.2 km and 70 vertical levels. This setup of the MetUM has previously proven reasonably accurate at simulating cases of cold-air outbreaks and polar lows in this region (e.g., Sergeev et al., 2017; Abel et al., 2017; Renfrew et al., 2019a, 2019b, 2021). Boundary conditions for the regional model simulations are provided by global operational MetUM simulations using a horizontal grid spacing of ~10 km, and these simulations are initialised from Met Office analysis data.

2.2 | Aircraft observations over Arctic sea ice

In-situ fluxes, 10-m neutral surface exchange coefficients and roughness lengths for momentum, heat, and moisture have been derived from aircraft observations along low-level flight legs (typically ~40 m in altitude), using the eddy covariance technique and standard atmospheric surface layer assumptions. For each flux observations we estimate the underlying sea-ice concentration based on albedo from surface shortwave radiation measurements following Elvidge et al. (2016). For further details on the acquisition, processing and quality control of these aircraft measurements, see E21.

Here we use observations in the vicinity of the MIZ to the north of Iceland and east of Greenland during seven flights undertaken between 28 February and 14 March 2018 as part of IGP. These flights were all conducted during relatively weak cold-air outbreak (CAO) conditions – that is, broadly northerly winds bringing cold air from the high Arctic across the MIZ and over the ocean – with associated upward turbulent heat fluxes (see Figure 2). These IGP observations generally occupy the aerodynamically *rough* regime (the mean R_{*i} is 257), with relatively strong winds over jagged, irregular sea ice (see E21). For further details on the IGP field campaign see Renfrew et al. (2019b) and for an evaluation of MetUM forecasts using IGP buoy, ship, and aircraft observations see Renfrew et al. (2021).

In Section 5, the IGP observations are supplemented with additional aircraft observations from the Barents Sea and Fram Strait, obtained during the *Aerosol-Cloud Coupling and Climate Interactions in the Arctic* (ACCACIA) field campaign of March 2013 (see Elvidge et al., 2016; noting that for technical reasons only the 'MASIN' Twin Otter aircraft observations are used in the present study). These ACCACIA observations are generally

characterised by a much lower aerodynamic roughness (mean R_{*i} of 8; see Figure 4c and 3d in E21).

In total, 303 surface flux observations are available for this study, with 107 from the IGP and 196 from ACCACIA. However, quality control reduces this number to 99 + 168, 88 + 154, and 74 + 159 for IGP + ACCACIA, and for momentum, heat, and moisture exchange, respectively.

2.3 | Experimental design

In this study, a statistical analysis is conducted of the IGP aircraft observations shown in Figure 2 and the MetUM sensitivity experiments that reproduce them. All observations were obtained between 10 and 17 UTC, and corresponding simulations are initialised on each day of observations at 00 UTC and run for 24-hours. The period between 6 and 18 UTC on 14 March 2018 (spanning the observations within the blue box in Figure 2) is identified as Case A and is subject to further analysis of the model output on broader spatial scales, as are two additional periods just outside of the period of IGP aircraft observations, identified as Cases B and C. Case B is a strong, persistent CAO event spanning a period of 60 hours from 1-4 April 2018. Case C is a warm-air intrusion (WAI) event (relatively warm air sourced from the lower latitudes advected over sea ice) spanning a period of 108 hours from 17-22 February 2018. The simulations covering these cases were initialised at 00 UTC on the first day of each case and run continuously until the end of each case (so for 72 hours and 120 hours for cases B and C, respectively).

2.4 | The surface exchange parameterisation configurations

Four parameterisation configurations are used for the surface exchange sensitivity experiments (Table 1, and listed below), comprising of two *control* configurations ($M_{Op}S_{Op}$ and $M_{IGP}S_{Op}$) and two *upgrade* configurations ($M_{IGP}S_{IGP}$ and $M_{IGP}S_{A87}$). Here 'M' denotes the momentum exchange setting and 'S' denotes the scalar exchange setting.

- $M_{Op}S_{Op}$ uses operational settings for both momentum and scalar exchange, i.e., z_{0i} = 5×10^{-4} m, $z_{0Ti}/z_{0i} = z_{0qi}/z_{0i}$ = 0.2 (Lock et al., 2021). Note these are the same settings

currently used operationally in all configurations (both global and regional) of the MetUM, including the RAL1-M configuration used for our simulations.

- $M_{IGP}S_{Op}$ uses operational settings for the scalar exchange component but has the momentum exchange component tuned to IGP conditions by setting z_{0i} to the median observed value of 10^{-2} m – far larger than in operational settings.
- $M_{IGP}S_{A87}$ again has the momentum component tuned optimally for IGP conditions and uses the *Blended A87* scheme for scalar exchange.
- $M_{IGP}S_{IGP}$ has both the momentum and scalar components tuned optimally for IGP conditions, with z_{0Ti}/z_{0i} and z_{0qi}/z_{0i} set to the median observed value of 3.9×10^{-4}.

The reason for tuning z_{0i} to the observations in three of the four configurations is to minimise biases in momentum exchange and, consequently, highlight the impact of parameterisation changes on scalar exchange. Recall this is necessary as SH and LH are dependent on z_{0i} and U – see equations (2), (3), (5) and (6) – and z_{0Ti} and z_{0qi} are also functions of z_{0i}. Note that the same IGP-derived value for z_{0i} is used for the case B and C simulations as the sea ice will be morphologically similar during these periods (c.f. Ponsoni et al., 2019).

Figure 3 illustrates our expectations for the model reproduction of surface exchange over the rough sea ice observed during IGP using each of the three primary parameterisation configurations (the two *control* configurations and $M_{IGP}S_{A87}$). It shows the observed exchange coefficients, binned by sea-ice concentration, overlaid by the functional forms of the parameterisations, where the exchange coefficients over seawater (ice concentration = 0) have been fixed to the median observed values, and U used in the *Blended A87* component of $M_{IGP}S_{A87}$ is set to the median observed value for each ice fraction bin.

For C_{DN}, $M_{IGP}S_{Op}$ and $M_{IGP}S_{A87}$ accurately reproduce the observed median values across all sea-ice concentrations due to the tuning of C_{DNi} to the median observed value, whilst $M_{Op}S_{Op}$ consistently underestimates these values, increasingly so at higher sea-ice concentrations. For C_{HN} and C_{EN}, $M_{IGP}S_{A87}$ reproduces the observed median values with reasonable accuracy, whilst $M_{IGP}S_{Op}$ consistently overestimates them, increasingly so with increasing sea-ice concentration. This highlights the need to consider the impact on scalar exchange when tuning for momentum exchange. Note that even $M_{IGP}S_{A87}$ fails to reproduce

the dip in C_{HN} and C_{EN} apparent in the observations for a sea-ice concentration of 1. However, the reliability of this specific bin of observations could be questioned, due to the low heat fluxes, as discussed in E21. Interestingly, $M_{Op}S_{Op}$ is functionally similar to $M_{IGP}S_{A87}$ for C_{HN} and C_{EN} and appears to match the observations comparably well. However, as we will explain in Section 5, this is the result of compensating errors in momentum and scalar roughness lengths, and this serendipitous performance will not occur in all aerodynamic roughness regimes.

3 | Validation of the *Blended A87* scheme in simulations of a persistent Arctic CAO over rough sea ice

In this section we evaluate the impact of the *Blended A87* scheme on MetUM skill in reproducing the surface exchanges and *rough* surface-layer conditions during the persistent CAO documented in the IGP aircraft observations (all data points shown in Figure 2). The observations depict northwesterly to northeasterly winds of mean speed 7.4 m s^{-1} bringing cold, dry air with a mean temperature of 260.7 K (-12.5 °C) and mean specific humidity of 1.2 g kg^{-1} over the generally warmer MIZ and ocean, with a mean surface temperature of 263.4 K (-9.8 °C) resulting in convective conditions in the ABL (Figure 2; Table 2). SH and LH have mean values of 17 and 13 W m^{-2}, respectively (Table 2), and generally peak just downwind of the MIZ, with a maximum total turbulent (sensible + latent) heat flux of 250 W m^{-2} (Figure 2).

Model experiments employing the $M_{IGP}S_{A87}$ configuration are tested against experiments employing each of the two *control* configurations ($M_{Op}S_{Op}$ and $M_{IGP}S_{Op}$). The results of these tests closely reflect expectations (as outlined in Section 2.4 and Figure 3) and are presented in Figures 4 and 5 and in Table 2.

In the $M_{IGP}S_{A87}$ and $M_{IGP}S_{Op}$ experiments, wind speeds are generally accurately reproduced (Figure 4b,c), with mean biases of 0.0 and 0.1 m s^{-1} and RMSE of 1.90 and 1.97 m s^{-1}, respectively (Figure 5; Table 2). In the $M_{Op}S_{Op}$ experiment, the wind speeds are generally overestimated, with a mean bias of 1.0 m s^{-1} resulting predominantly from overestimates at higher sea-ice concentrations and higher wind speeds (Figure 4a), and a greater RMSE of 2.71 m s^{-1}. These results closely reflect expectations; overestimates in

$M_{Op}S_{Op}$ wind speeds reflecting negative biases in surface drag that increase with increasing sea-ice concentration (Figure 3a).

In the $M_{IGP}S_{A87}$ and $M_{Op}S_{Op}$ experiments, air temperatures are generally accurately reproduced (Figure 4d,f), with negligible mean biases (both 0.0 K) and RMSE of 1.05 and 1.03 K, respectively (Figure 5; Table 2). In the $M_{IGP}S_{Op}$ experiment, the temperatures are generally overestimated, with a mean bias of 0.8 K resulting predominantly from overestimates at higher sea-ice concentrations and consequently lower temperatures (Figure 4e), as well as a greater RMSE of 1.23 K. Again, these results closely reflect expectations; overestimates in $M_{IGP}S_{Op}$ air temperatures reflecting positive (upward) biases in surface heat exchange that increase with increasing sea-ice concentration (Figure 3b). These heat exchange biases are seen in the MetUM output, with a mean positive bias in SH of 25 W m^{-2} meaning too much heat transfer from the ocean into the cooler air. In the $M_{IGP}S_{A87}$ and $M_{Op}S_{Op}$ experiments, these mean biases are smaller: 11 and 14 W m^{-2}, respectively (Figure 5; Table 2).

The sensitivity in surface temperature matches that for air temperature, with a mean positive bias that is largest in the $M_{IGP}S_{Op}$ experiment at 1.4 K, and smaller in the $M_{IGP}S_{A87}$ and $M_{Op}S_{Op}$ experiments at 0.8 and 0.9 K, respectively. This difference is due to the warm bias in air temperatures in $M_{IGP}S_{Op}$ translating to a warm bias in surface temperatures via a corresponding bias in surface heat exchange over the ice portion of model grid cells, noting that the surface temperature of seawater is prescribed in these atmosphere-only simulations (and, in reality, changes far slower than does ice surface temperature).

In contrast to wind speed and temperature, model performance for atmospheric humidity does not match expectations. There are significant (negative) mean biases for specific humidity in all the model experiments, with the smallest bias being in the $M_{IGP}S_{Op}$ experiment – the opposite of that expected (see Figure 3c). This is due to a compensating error related to widespread negative model biases in humidity inherited from the global model simulations. This humidity bias is apparent in IGP observations obtained far from the MIZ (over the northeastern Iceland Sea; not shown) and has previously been reported by Renfrew et al. (2021). Despite this bias, the model performance for LH is broadly as expected, with a mean positive bias in all experiments that is greatest in the $M_{IGP}S_{Op}$ experiment. This larger positive LH bias in the $M_{IGP}S_{Op}$ experiment is the compensating error that leads, via upward moisture transfer, to the smaller negative humidity bias in this

experiment. Note that a subsample of the data for which the model bias in specific humidity is small (< 0.1 g kg^{-1}) exhibits smaller biases in LH in all model experiments, including a very small mean bias (1 W m^{-2}) in the $M_{IGP}S_{A87}$ experiment.

Table 2 also summarises the performance of the $M_{IGP}S_{IGP}$ model experiment (recall this uses fixed observed values for z_{0Ti} and z_{0qi}). Comparing its performance with that of $M_{IGP}S_{A87}$ reveals the importance of wind speed sensitivity in the *Blended A87* scheme, noting that if U in equation 11 is fixed to the median value from all the observations, then the values of z_{0Ti}/z_{0i} and z_{0qi}/z_{0i} derived using the the A87 theoretical model are very close to the median observed value of 3.9×10^{-4} that is used in the $M_{IGP}S_{IGP}$ experiment. The biases and RMSE for this experiment are very similar to those of the $M_{IGP}S_{A87}$ experiment, implying that the variability in wind speed in our IGP observations is relatively unimportant to the heat and moisture fluxes derived from the *Blended A87* scheme.

4 | Sensitivity of the Arctic atmospheric boundary layer to surface scalar exchange over rough sea ice

In this section we focus on the three case studies – Cases A, B and C – to explore the impact of the *Blended A87* scheme on the Arctic ABL in different meteorological regimes. Figure 6 shows instantaneous mean sea level pressure and boundary-layer wind vectors from the $M_{IGP}S_{A87}$ experiments at times that are broadly representative of conditions at the "peak" (in terms of wind strength) of each case study. During "peak" conditions in Case A, a weak, zonally-oriented high-pressure ridge weakening eastward is associated with relatively weak northwesterly winds bringing cold air across the MIZ in the north of the model domain and weak northeasterly winds in the south of the domain. During "peak" conditions in Case B, a low-pressure system in the eastern Iceland Sea and broadly northwest-to-southeast pressure gradients are associated with strong northerly-to-northeasterly winds bringing cold air across the entire model domain. During "peak" conditions in Case C, a pressure gradient from the eastern Iceland Sea to the Denmark Strait drives southerly winds bringing relatively warm air from lower latitudes across the MIZ. Of the two CAO cases (A and B), Case B is simpler to analyse due to the relative homogeneity of the wind field – broadly northerly winds – across the entire model domain. For Case C, the sensitivity of conditions to surface

exchange parameterisation is relatively small in most diagnostics. Consequently, we now focus on Case B, although we return to Cases A and C later.

Figure 7 shows the differences between the $M_{IGP}S_{A87}$ experiment and the two *control* experiments in key diagnostics over consolidated/pack ice (light grey), the MIZ (dark grey) and open water (black) within the *target* region (defined as the region enclosed by the red dashed line in Figure 6), time-averaged over the 60-hour duration of Case B. As with the results of Section 3, these differences broadly align with expectations. Figures 8, 9 and 10 provide spatial context to the results illustrated in Figure 7, showing map plots and roughly-meridional-oriented cross sections of key diagnostics at the time of "peak" Case B conditions.

The most notable differences between the $M_{IGP}S_{A87}$ and $M_{Op}S_{Op}$ experiments are in the winds (Figure 7a). Mean wind speed in the *target* region is ~0.7 m s^{-1} weaker over pack ice and the MIZ in the $M_{IGP}S_{A87}$ experiment, reflecting enhanced surface drag over these surfaces (c.f. Figure 3a). The mean difference over the open ocean is smaller (~0.25 m s^{-1} lower in the $M_{IGP}S_{A87}$ experiment), however Figure 8 shows significant instantaneous wind speed differences elsewhere over the ocean, both within and above the ABL. This includes a relative weakening of a low-level wind jet that emerges from the Peninsula south of the Scoresby Sund Fjord and extends southwards; and a relative strengthening of the northerly winds over the Iceland Sea to the east of the transect line in Figure 8.

Between the $M_{IGP}S_{A87}$ and $M_{IGP}S_{Op}$ experiments, the differences in wind speed are generally small, but there are significant differences in the other key diagnostics (Figure 7b). Mean air temperature and humidity within the *target* region are lower in the $M_{IGP}S_{A87}$ experiment over all three surface types, but most so over the MIZ, with differences of ~1.2 K and ~0.1 g kg^{-1}, respectively. These differences in air temperature and humidity correspond with differences in mean sensible and latent heat fluxes, which are lower in the $M_{IGP}S_{A87}$ experiment by 31 and 13 W m^{-2}, respectively, over the MIZ, owing to smaller surface scalar exchange coefficients (c.f. Figure 3).

Figure 9 shows potential temperature maps and cross sections illustrating the typical ABL structure seen during a CAO (e.g., Renfrew and Moore, 1999). The surface exchange experiments clearly show significant differences in the structure of the inversion-capped ABL as it evolves and deepens downwind of the MIZ. Significant differences in potential temperature (of at least 0.5 K; Figure 9b) and specific humidity (not shown) persist in the

ABL for hundreds of km downwind of the MIZ. Due to weaker upward sensible heat fluxes (Figure 10a,c), the ABL warms at a slower rate over the pack ice and MIZ in the $M_{IGP}S_{A87}$ experiment, than the $M_{IGP}S_{Op}$ experiment, so at the sea-ice edge the near-surface air temperature is up to 2 K cooler and is cooler for hundreds of km downwind (Figure 9b). This makes the air-sea temperature gradient in the $M_{IGP}S_{A87}$ experiment larger, resulting in larger upward SH fluxes over the ocean; as a consequence, the ABL temperature increases at a faster rate between the sea-ice edge and ~300 km downwind along the transect and the ABL is 100-300 m deeper (Figure 9).

Mean surface temperature over sea ice in the *target* region is significantly lower in the $M_{IGP}S_{A87}$ experiment than in the $M_{IGP}S_{Op}$ experiment; ~0.7 K lower over pack ice, and ~0.6 K lower over the MIZ (Figure 7). Figure 10d shows that this deficit can reach 1.5 K in some regions.

Figures 11 and 12 replicate Figure 7, but for Cases A and C, respectively. The case-mean sensitivities shown in Figure 11 for the CAO conditions of Case A are qualitatively and quantitatively similar to those for the CAO conditions of Case B. This reflects the fact that although Case B was stronger (in terms of wind strength) at its "peak" (see Figure 6), it was more intermittent over its duration than Case A. For the WAI event of Case C, qualitatively similar differences are apparent between the $M_{IGP}S_{A87}$ and $M_{Op}S_{Op}$ experiments, with significantly weaker mean wind speeds in the former, by 0.5-0.6 m s^{-1} over pack ice and the MIZ. However, the differences between the $M_{IGP}S_{A87}$ and $M_{IGP}S_{Op}$ are far smaller. During Case C, warm on-ice advection results in statically stable conditions over the sea ice, which suppresses turbulence and leads to relatively weak heat fluxes directed downwards into the ice. The weakened fluxes lead to only modest differences in air temperature, humidity and surface heat fluxes between the WAI model sensitivity experiments (Figure 12). There is a more significant difference in surface temperature over pack ice – albeit a reduced one relative to cases A and B – again with the lower mean value in the $M_{IGP}S_{A87}$ experiment, by ~0.4 K over pack ice. This is a result of reduced downward surface heat transfer over ice in the $M_{IGP}S_{A87}$ experiment (c.f. Figure 3). It should be noted though that the mean surface sensible heat flux over pack ice is not, as might be expected, greater in the $M_{IGP}S_{A87}$ experiment. This appears to be a result of the downward fluxes over ice competing with larger but less widespread upward fluxes over open water within the MIZ (that do not affect the prescribed sea surface temperature).

5 | Wider implications

In Sections 3 and 4 it has been shown that introducing aerodynamic-roughness dependence to surface scalar exchange over sea ice in aerodynamically *rough* conditions results in significant changes in simulations of the Arctic ABL over and downwind of sea ice, and that doing so is vital if z_{0i} is allowed to vary regionally in a physically realistic way. These findings match our expectations based on an analysis of the surface exchange coefficients derived using simplified ("offline") forms of the parameterisation schemes. However, our simulations have been limited to *rough* conditions. In this section we extend our analysis of the "offline" parameterisations to explore the behaviour of sea-ice surface exchange parameterisation configurations across the full range of plausible aerodynamic roughness conditions.

Figure 13 shows the surface exchange coefficients over sea ice as functions of R_{*i} for both IGP and ACCACIA aircraft observations, and for the $M_{Op}S_{Op}$, $M_{IGP}S_{Op}$ and $M_{IGP}S_{A87}$ parameterisation schemes. The observations are binned by R_{*i}, and include all those where the observed sea-ice fraction is >0.5. We use this threshold to obtain a larger set of observations, and so a more robust analysis, with the justification that similar mean values are found for higher sea-ice fraction thresholds.

For the $M_{Op}S_{Op}$ scheme, the surface exchange coefficients do not vary with R_{*i} as all roughness lengths are fixed. For the $M_{IGP}S_{Op}$ scheme, sensitivity to R_{*i} is present only through variability in z_{0i} (c.f. Equation (10)), with z_{0i} being set in each R_{*i} bin to the median observed value. For the $M_{IGP}S_{A87}$ scheme, sensitivity to R_{*i} is due both to variability in z_{0i} and in $\frac{z_{0Ti}}{z_{0i}}$ and $\frac{z_{0qi}}{z_{0i}}$ through the A87 theoretical model. Since C_{DNi} varies only with z_{0i}, the functional forms of $M_{IGP}S_{Op}$ and $M_{IGP}S_{A87}$ pass directly through the bin-median C_{DNi} observations (Figure 13a). Moreover, given that variability in R_{*i} is dominated by that in z_{0i} (see Figure 5e in E21), the relationship between C_{DNi} and R_{*i} shown in Figure 13a is dominated by self-correlation. Note this is not the case for the relationships between the scalar exchange coefficients and R_{*i} shown in Figure 13b,c (as established in E21; their Appendix A).

For most of the *rough* regime (R_{*i} > ~10), Figure 13 corroborates the parameterisation performance results discussed earlier in this study. The $M_{Op}S_{Op}$ scheme is shown to underestimate surface drag (Figure 13a), and to relatively accurately reproduce surface scalar exchange (Figure 13b,c). The latter is, as previously mentioned, a result of compensating errors; z_{0i} is too small and so, according to (5) and (6), z_{0Ti} and z_{0qi} must be too large. The $M_{IGP}S_{Op}$ scheme corrects the surface drag but considerably overestimates the surface scalar exchange in the rough regime. The $M_{IGP}S_{A87}$ scheme not only corrects the surface drag but also reproduces both surface scalar exchange coefficients to a relatively accurate degree; biases in C_{HNi} and C_{ENi} being less than half the respective observed median values for each R_{*i} bin (with the exception of one bin – that of $10^4 < R_{*i} < 10^5$ – for C_{HNi}, though note there is only one observational data point in this bin).

For *smooth* and *transitional* conditions (R_{*i} < 2.5), z_{0Ti} and z_{0qi} are, in observations (e.g. Andreas et al., 1987, 2010; E21) and in theory (Andreas et al., 1987), roughly proportional to z_{0i}, and so setting $\frac{z_{0Ti}}{z_{0i}}$ and $\frac{z_{0qi}}{z_{0i}}$ to constants is appropriate (see Figure 2). Consequently, as illustrated in Figure 13, the $M_{IGP}S_{Op}$ and $M_{IGP}S_{A87}$ schemes perform well for both surface drag and scalar exchange for *smooth* and *transitional* conditions. The $M_{Op}S_{Op}$ scheme on the other hand overestimates both surface drag and scalar exchange, due to the overestimated z_{0i} and consequently also overestimated z_{0Ti} and z_{0qi}. Note there is a convergence in all three parameterisation schemes and the observations at R_{*i} ~6 in Figure 13. Here, the values assigned operationally in the MetUM for z_{0i}, $\frac{z_{0Ti}}{z_{0i}}$ and $\frac{z_{0qi}}{z_{0i}}$ are all appropriate, likely reflecting previous intentional tuning of these parameters to this moderate R_{*i} value.

Recall the results shown in Figure 13 pertain only to conditions over consolidated sea ice; however, Figure 3 demonstrates that, for the most part, the performance of the surface exchange schemes over consolidated sea ice qualitatively reflects their performance over lower sea-ice concentrations. Therefore, the parameterisation implications discussed in this section can be considered qualitatively representative of surface exchange over any ocean model grid cell containing sea ice.

Figure 13 and the analysis presented in this section encapsulates that the surface exchange scheme currently operational in the MetUM is only appropriate for both momentum and scalar exchange across a narrow range of aerodynamic roughness

conditions. Optimising this scheme for surface momentum exchange whilst keeping its handling of scalar exchange the same (with z_{0Ti} and z_{0qi} changing linearly with changes in z_{0i}) widens this range to include the lower aerodynamic roughnesses (the *smooth* and *transitional* regimes) but is hugely detrimental to the reproduction of scalar exchange at the higher aerodynamic roughnesses (the *rough* regime). This is because whilst in the *smooth* regime a change in z_{0i} changes both momentum and scalar exchange through skin friction; in the *rough* regime a change in z_{0i} changes surface-layer pressure gradients, which directly affects momentum exchange through form drag but not, in theory, the scalar exchanges. As illustrated here, a parameterisation that accounts for the aerodynamic roughness, such as the *Blended A87* scheme, is necessary for accurate reproduction of both momentum and scalar exchange across the full range of roughnesses.

6 | Discussion and conclusions

Turbulence in the atmospheric boundary layer (ABL) provides a pathway through which physical and chemical constituents are exchanged between the atmosphere and the frozen oceans of the polar regions. This air-sea-ice 'communication' is a vital component of the polar and global climate systems and is chiefly governed by the concentration and properties of sea ice. Recent advances in our understanding of the drag exerted by sea ice on the atmosphere, via both skin drag from surface friction and form drag from ice floe edges, have led to improved representation of surface momentum exchange over sea ice in numerical weather and climate models. However, the treatment of surface scalar (notably heat and moisture) exchange over sea ice in such models has remained crude. In this study, we have tested a new parameterisation for this scalar exchange in a state-of-the-art NWP model (the MetUM); the *Blended A87* scheme, which accounts for the important influence of aerodynamic roughness (i.e., the roughness Reynolds number, R_*) on the relationship between scalar and momentum exchange over consolidated sea ice, in line with long-standing theory and recent field observations.

We have tested the impact of the new *Blended A87* scheme in the MetUM using in-situ aircraft-derived surface-layer turbulence observations and MetUM simulations of a persistent cold-air outbreak (CAO) characterised by cool, northerly winds over the Iceland

and Greenland Seas. The observations were obtained as part of the field campaign of the Iceland-Greenland Seas Project (IGP).

In the sea ice surface exchange scheme currently operational in the MetUM, the exchange coefficients for both momentum and the scalars are functions of sea-ice concentration only (i.e., z_{0i}, $\frac{z_{0Ti}}{z_{0i}}$ and $\frac{z_{0qi}}{z_{0i}}$ are fixed). This crude treatment of surface exchange over consolidated sea ice is unphysical outside of a narrow range of R_{*i} values. In aerodynamically *rough* conditions, momentum exchange is generally underestimated, as revealed by a positive mean wind speed bias of ~1 m s^{-1} (against aircraft observations) in operational MetUM simulations; however, owing to compensating errors in the roughness lengths for momentum and the scalars, scalar exchange is reproduced with reasonable accuracy. In aerodynamically *smooth* conditions, we demonstrate that overestimates in both surface momentum and scalar exchange are to be expected; although we have not explored this in the context of full MetUM simulations here.

To isolate model sensitivities to the scalar component of the surface exchange scheme, and in anticipation of future advances in the treatment of surface roughness due to sea ice topography, we have run additional MetUM simulations in which momentum exchange over consolidated sea ice is optimised by prescribing z_{0i} from the IGP observations. We show that replacing the operational treatment for scalar exchange with the *Blended A87* scheme yields substantial improvements in model skill; reducing mean biases in surface sensible heat flux, surface latent heat flux, air temperature and surface temperature from 25 to 11 W m^{-2}, 22 to 12 W m^{-2}, 0.8 to 0.0 K, and 1.4 to 0.8 K, respectively. We have demonstrated that these improvements are predominantly the result of the new scheme's sensitivity to z_{0i}, via R_{*i}, and that its sensitivity to wind speed is of secondary importance.

To explore the broader impact of the *Blended A87* scheme on ABL conditions, we have employed MetUM sensitivity experiments focused on three case studies over the Iceland and Greenland Seas. In simulations of a strong, long-lived CAO case, replacing the operational scalar exchange treatment with the *Blended A87* scheme causes a reduction in the time-averaged total surface turbulent heat flux over the MIZ (consolidated ice) of 44 (16) W m^{-2} – 20% (50%) of the mean in the operational simulation – and corresponding reductions in low-level air temperature and surface temperature of 1.2 (0.3) K and 0.6 (0.7)

K, respectively. Furthermore, significant changes in the properties and structure of the ABL are apparent for hundreds of km downwind of the MIZ. In simulations of a long-lived warm air intrusion, the impact of the new scheme is generally much smaller, owing to the suppression of ABL turbulence under conditions of elevated static stability, except for on surface temperature.

There may be scope for extending the *Blended A87* scheme to incorporate the effect of turbulence generated over ice floe edges, e.g. using the framework suggested by Lüpkes and Gryanik (2015). However, further work is required using observations to verify the physical basis for this.

The results of this study demonstrate that introducing aerodynamic-roughness dependence to the parameterisation of surface scalar exchange over sea ice through the implementation of the *Blended A87* scheme has the potential for considerable improvements in the prediction of polar weather and climate, and consequently of surface temperature and sea ice. This is particularly the case under aerodynamically *rough* conditions, which have recently been found to characterise a large proportion of sea ice in the Arctic Ocean (albeit based on ship measurements that are limited to the MIZ) (Srivastava et al., 2022). However, to fully harness these benefits in global model simulations, it will be necessary to represent spatiotemporal variability in the topography of consolidated sea ice on aerodynamic roughness. This remains a major challenge for the modelling of surface fluxes over sea ice.

Acknowledgements

This paper was made possible by funding provided by NERC under the project grant 'CANDIFLOS' (NE/S000453/1 and NE/S000690/1). It uses aircraft-based observations from the NERC grants NE/I028297/1 and NE/N009754/1, which funded the ACCACIA and IGP field campaigns, respectively. We would like to thank all campaign participants who contributed to obtaining those observations. These aircraft observations are available at CEDA via British Antarctic Survey (2014) for the ACCACIA dataset, and via Renfrew (2019) for IGP dataset. The MetUM simulations were carried out on MONSooN, a collaborative facility supplied under the Joint Weather and Climate Research Programme, a strategic partnership between the Met Office and the Natural Environment Research Council. The MetUM data are

available on the Met Office Managed Archive Storage System (MASS) and available on request. Visualisation software used: MATLAB and Python packages Cartopy v0.17 (16 November 2018, Met Office, UK, https://github.com/SciTools/cartopy/archive/v0.17.0.tar.gz) and Iris v2.2 (11 October 2018, Met Office, UK, https://github.com/SciTools/iris/archive/v2.2.0.tar.gz). This study is a contribution to the Year of Polar Prediction (YOPP), a flagship activity of the Polar Prediction Project, initiated by the World Weather Research Programme of the World Meteorological Organisation.

References

Andreas, E.L., 1987. A theory for the scalar roughness and the scalar transfer coefficients over snow and sea ice. *Boundary-Layer Meteorology*, **38**(1-2), pp.159-184.

Andreas, E.L., Horst, T.W., Grachev, A.A., Persson, P.O.G., Fairall, C.W., Guest, P.S. and Jordan, R.E., 2010. Parametrizing turbulent exchange over summer sea ice and the marginal ice zone. *Quarterly Journal of the Royal Meteorological Society*, **136**(649), pp.927-943.

Arya, S.P.S., 1973. Contribution of form drag on pressure ridges to the air stress on Arctic ice. *Journal of Geophysical Research*, **78**(30), pp.7092-7099.

Arya, S.P.S., 1975. A drag partition theory for determining the large-scale roughness parameter and wind stress on the Arctic pack ice. *Journal of Geophysical Research*, **80**(24), pp.3447-3454.

Birnbaum, G. and Lüpkes, C., 2002. A new parameterization of surface drag in the marginal sea ice zone. *Tellus A: Dynamic Meteorology and Oceanography*, **54**(1), pp.107-123.

British Antarctic Survey (2014): British Antarctic Survey Twin Otter aircraft Meteorological Airborne Science INstrumentation (MASIN) core data for the Aerosol Cloud Coupling and Climate Interactions in the Arctic (ACCACIA) project.. NCAS British Atmospheric Data Centre, 04 March 2021. doi:10.5285/0844186db1ba9e20319a2560f8d61651.

Bush, M., Allen, T., Bain, C., Boutle, I., Edwards, J., Finnenkoetter, A., ... & Zerroukat, M. (2020). The first Met Office unified model–JULES regional atmosphere and land configuration, RAL1. Geoscientific Model Development, 13(4), 1999-2029.

Castellani, G., Lüpkes, C., Hendricks, S. and Gerdes, R., 2014. Variability of Arctic sea-ice topography and its impact on the atmospheric surface drag. *Journal of Geophysical Research: Oceans*, **119**(10), pp.6743-6762.

Claussen, M. (1990). Area-averaging of surface fluxes in a neutrally stratified, horizontally inhomogeneous atmospheric boundary layer. Atmospheric Environment. Part A. General Topics, 24(6), 1349-1360.

Elvidge, A., Renfrew, I., Weiss, A.I., Brooks, I.M., Lachlan-Cope, T.A. and King, J.C., 2016. Observations of surface momentum exchange over the marginal ice zone and recommendations for its parametrisation. *Atmospheric Chemistry and Physics*, **16**, pp.1545-1563.

Elvidge, A. D., Renfrew, I. A., Brooks, I. M., Srivastava, P., Yelland, M. J., & Prytherch, J. (2021). Surface heat and moisture exchange in the marginal ice zone: Observations and a new parameterization scheme for weather and climate models. Journal of Geophysical Research: Atmospheres, 126(17), e2021JD034827.

Fichefet, T. and Maqueda, M.M., 1997. Sensitivity of a global sea ice model to the treatment of ice thermodynamics and dynamics. *Journal of Geophysical Research: Oceans*, **102**(C6), pp.12609-12646.

Fitzpatrick, N., Radić, V., & Menounos, B. (2019). A multi-season investigation of glacier surface roughness lengths through in situ and remote observation. The Cryosphere, 13(3), 1051-1071.

Garbrecht, T., Lüpkes, C., Hartmann, J. and Wolff, M., 2002. Atmospheric drag coefficients over sea ice–validation of a parameterisation concept. *Tellus A: Dynamic Meteorology and Oceanography*, **54**(2), pp.205-219.

Jung, T., Gordon, N. D., Bauer, P., Bromwich, D. H., Chevallier, M., Day, J. J., ... & Yang, Q. (2016). Advancing polar prediction capabilities on daily to seasonal time scales. Bulletin of the American Meteorological Society, 97(9), 1631-1647.

Lock, A., Edwards, J. and Boutle, I., 2021. Unified Model Documentation Paper 24: The Parametrization of Boundary Layer Processes. Met Office Technical Description MetUM Version 12.2. UK Met Office, Exeter (UK), p.75.

Lüpkes, C. and Birnbaum, G., 2005. Surface drag in the Arctic marginal sea-ice zone: a comparison of different parameterisation concepts. *Boundary-layer meteorology*, **117**(2), pp.179-211.

Lüpkes, C. and Gryanik, V.M., 2015. A stability-dependent parametrization of transfer coefficients for momentum and heat over polar sea ice to be used in climate models. *Journal of Geophysical Research: Atmospheres*, **120**(2), pp.552-581.

Lüpkes, C., Gryanik, V.M., Hartmann, J. and Andreas, E.L., 2012. A parametrization, based on sea ice morphology, of the neutral atmospheric drag coefficients for weather prediction and climate models. *Journal of Geophysical Research: Atmospheres*, **117**(D13).

Monin, A. S., & Obukhov, A. M. (1954). Basic laws of turbulent mixing in the surface layer of the atmosphere. Contrib. Geophys. Inst. Acad. Sci. USSR, 151(163), e187.

Overland, J., Dunlea, E., Box, J. E., Corell, R., Forsius, M., Kattsov, V., ... & Wang, M. (2019). The urgency of Arctic change. *Polar Science*, **21**, 6-13.

Petty, A. A., M. C. Tsamados, and N. T. Kurtz (2017), Atmospheric form drag coefficients over Arctic sea ice using remotely sensed ice topography data, spring 2009–2015, *J. Geophys. Res. Earth Surf*., **122**, 1472–1490, doi:10.1002/2017JF004209.

Ponsoni, L., Massonnet, F., Fichefet, T., Chevallier, M., & Docquier, D. (2019). On the timescales and length scales of the Arctic sea ice thickness anomalies: a study based on 14 reanalyses. The Cryosphere, 13(2), 521-543.

Pope, J.O., Bracegirdle, T.J., Renfrew, I.A. and Elvidge, A.D., 2020. The impact of wintertime sea-ice anomalies on high surface heat flux events in the Iceland and Greenland Seas. Climate Dynamics, **54**(3), pp.1937-1952.

Rae, J.G.L., Hewitt, H.T., Keen, A.B., Ridley, J.K., Edwards, J.M. and Harris, C.M., 2014. A sensitivity study of the sea ice simulation in the global coupled climate model, HadGEM3. *Ocean Modelling*, **74**, pp.60-76.

Raphael, M. N. (2007). The influence of atmospheric zonal wave three on Antarctic sea ice variability. Journal of Geophysical Research: Atmospheres, 112(D12).

Renfrew, I.A. 2019: In situ observations of air-sea interaction processes from the Iceland Greenland seas Project (IGP). Centre for Environmental Data Analysis, 04 March 2021. http://catalogue.ceda.ac.uk/uuid/b3e807b8df824a8ca83468ce2e5b54e5

Renfrew, I. A., & Moore, G. W. K. (1999). An extreme cold-air outbreak over the Labrador Sea: Roll vortices and air–sea interaction. Monthly Weather Review, 127(10), 2379-2394.

Renfrew, I.A., Elvidge, A.D. and Edwards, J.M., 2019a. Atmospheric sensitivity to marginal-ice-zone drag: Local and global responses. *Quarterly Journal of the Royal Meteorological Society*, **145**(720), pp.1165-1179.

Renfrew, I.A., Pickart, R.S., Våge, K., Moore, G.W.K., Bracegirdle, T.J., Elvidge, A.D., et al., 2019b: The Iceland Greenland Seas Project, *Bulletin of the American Meteorological Society,* **100,** 1795–1817. DOI:10.1175/BAMS-D-18-0217.1

Renfrew, I.A., Barrell, C., Elvidge, A.D., Brooke, J.K., Duscha, C., King, J.C., Kristiansen, J., Cope, T.L., Moore, G.W.K., Pickart, R.S. and Reuder, J., 2021. An evaluation of surface meteorology and fluxes over the Iceland and Greenland Seas in ERA5 reanalysis: The impact of sea ice distribution. *Quarterly Journal of the Royal Meteorological Society*, **147,** 691–712. DOI:10.1002/qj.3941

Roberts, C. D., Senan, R., Molteni, F., Boussetta, S., Mayer, M., & Keeley, S. P. (2018). Climate model configurations of the ECMWF Integrated Forecasting System (ECMWF-IFS cycle 43r1) for HighResMIP. *Geoscientific model development*, **11**(9), 3681-3712.

Sergeev, D. E., Renfrew, I. A., Spengler, T., & Dorling, S. R. (2017). Structure of a shear-line polar low. Quarterly Journal of the Royal Meteorological Society, 143(702), 12-26.

Sigmond, M., Fyfe, J. C., & Swart, N. C. (2018). Ice-free Arctic projections under the Paris Agreement. Nature Climate Change, 8(5), 404-408.

Srivastava, P., Brooks, I. M., Prytherch, J., Salisbury, D. J., Elvidge, A. D., Renfrew, I. A., & Yelland, M. J. (2022a). Ship-based estimates of momentum transfer coefficient over sea ice and recommendations for its parameterization. Atmospheric Chemistry and Physics, 22(7), 4763-4778.

Stössel, A., Cheon, W.G. and Vihma, T., 2008. Interactive momentum flux forcing over sea ice in a global ocean GCM. *Journal of Geophysical Research: Oceans*, **113**(C5). DOI:10.1029/2007JC004173

Tsamados, M., Feltham, D.L., Schroeder, D., Flocco, D., Farrell, S.L., Kurtz, N., Laxon, S.W. and Bacon, S., 2014. Impact of variable atmospheric and oceanic form drag on simulations of Arctic sea ice. *Journal of Physical Oceanography*, **44**(5), pp.1329-1353.

Vavrus, S. and Harrison, S.P., 2003. The impact of sea-ice dynamics on the Arctic climate system. *Climate Dynamics*, **20**(7-8), pp.741-757.

Vihma, T. (1995). Subgrid parameterization of surface heat and momentum fluxes over polar oceans. Journal of Geophysical Research: Oceans, 100(C11), 22625-22646.

Vihma, T., Johansson, M. M., & Launiainen, J. (2009). Radiative and turbulent surface heat fluxes over sea ice in the western Weddell Sea in early summer. Journal of Geophysical Research: Oceans, 114(C4).

Yu, X., Rinke, A., Dorn, W., Spreen, G., Lüpkes, C., Sumata, H. and Gryanik, V.M., 2020. Evaluation of Arctic sea ice drift and its dependency on near-surface wind and sea ice conditions in the coupled regional climate model HIRHAM–NAOSIM. *The Cryosphere*, **14**(5), pp.1727-1746.

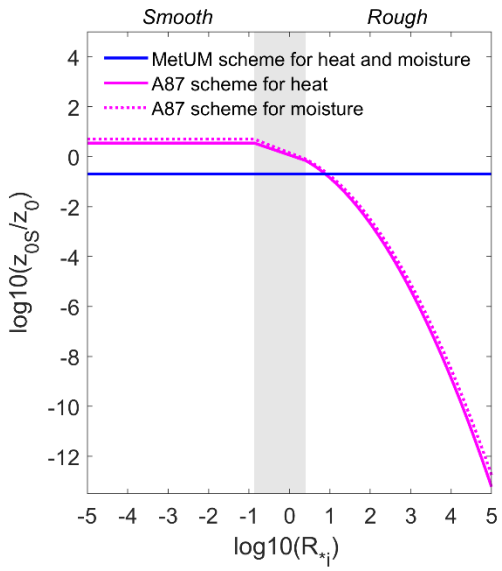

Figure 1 | Functional forms of the surface scalar flux algorithms over sea ice, in terms of the relationship between $\frac{z_{0Si}}{z_{0i}}$ and R_{*i}, where z_{0Si} is the surface roughness length for scalar quantities (i.e., z_{0Ti} for heat, or z_{0qi} for moisture) and $R_{*i} = \frac{z_{0i}\, u_{*i}}{\nu}$ is the roughness Reynolds number. The functional forms shown are from the surface exchange schemes used operationally in the MetUM and in the conceptual model of Andreas (1987). Gray background shading marks the *transitional* aerodynamic roughness regime, to the left of which ($R_* \leq 0.135$) is the *smooth* regime, and to the right of which ($R_* \geq 2.5$) is the *rough* regime.

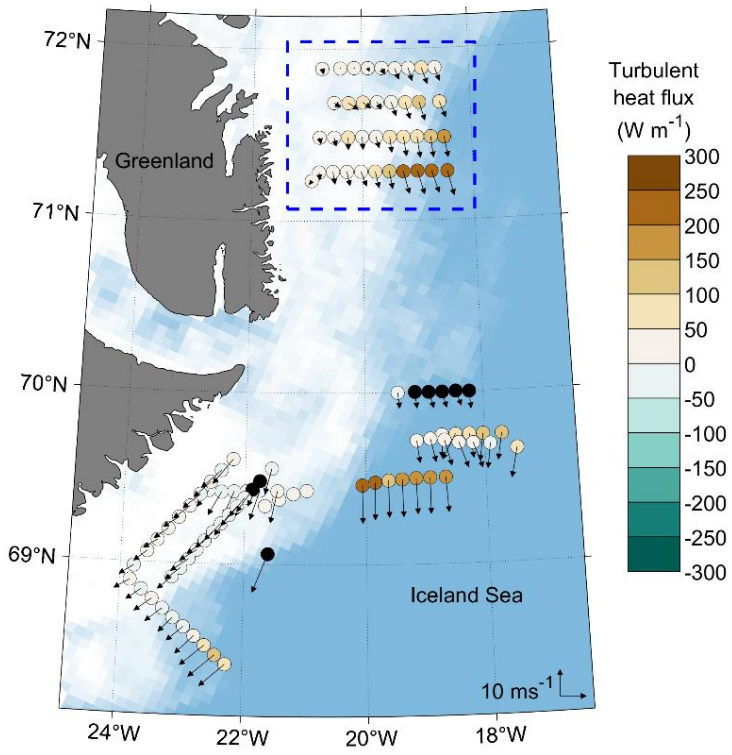

Figure 2 | Map encompassing the domain used for the regional MetUM simulations, covering the northern Iceland Sea, the southwestern Greenland Sea and the east coast of Greenland. Aircraft observations from seven IGP flights are denoted by circles with shading for total turbulent heat fluxes (positive values denoting upward fluxes) and wind vectors as arrows. The campaign-average sea-ice concentration is shown as blue-to-white shading. Black dots show data points for which the turbulent heat flux is not available, either due to instrument failure (e.g., the five points along 70°N, for which latent heat fluxes are not available) or failure to pass quality control. The box marked by blue dashed lines encloses the observations that document Case A. This figure is adapted from Figure 1 in E21.

	The parameterisation of momentum exchange over sea ice and the MIZ		**The parameterisation of scalar exchange over sea ice and the MIZ**	
$M_{OP}S_{OP}$	z_{0i} set to operational value of 5×10^{-4} m	τ derived using equations (1), (4) and (7); τ_f derived using the Lupkes et al. (2012) scheme with parameter settings from Elvidge et al., (2016)	z_{0Ti}/z_{0i} and z_{0qi}/z_{0i} set to operational value of 0.2	SH and LH derived using equations (2), (3), (5), (6), (8) and (9)
$M_{IGP}S_{OP}$	z_{0i} set to median observed value from IGP of 10^{-2} m			
$M_{IGP}S_{IGP}$			z_{0Ti}/z_{0i} and z_{0qi}/z_{0i} set to median observed value from IGP of 3.9×10^{-4}	
$M_{IGP}S_{A87}$			z_{0Ti}/z_{0i} and z_{0qi}/z_{0i} derived as a function of R_* using Blended A87 scheme (from E21)	

Table 1 | Overview of the four model configurations used for the parameterisation of surface exchange over sea ice and the MIZ

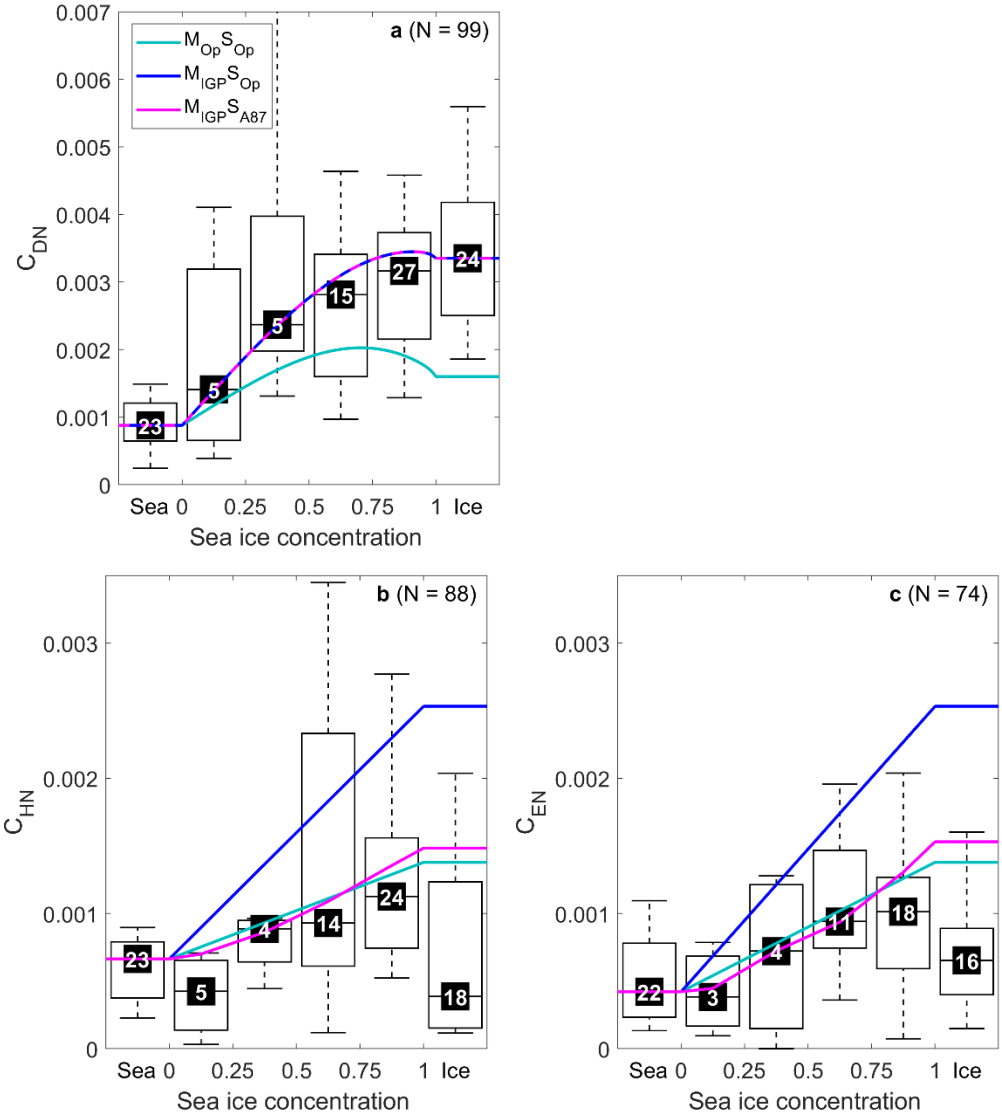

Figure 3 | Surface exchange coefficients for a) momentum, b) heat and c) moisture as functions of sea-ice concentration for the IGP aircraft observations and for the $M_{Op}S_{Op}$, $M_{IGP}S_{Op}$ and $M_{IGP}S_{A87}$ sea ice surface exchange parameterisation schemes. Panels show observations as box and whiskers plots with the median (horizontal line), interquartile range (open box) and 10th and 90th percentiles (whiskers) for the following sea-ice concentration bins: 0 ("sea"), 0–0.25, 0.25–0.5, 0.5–0.75, 0.75–1, and 1 ("ice"). The number of data points in each bin is shown at the median value. For the parameterisation schemes, C_{HNw} and C_{ENw} (i.e., C_{HN} and C_{EN} in the sea bin) are set to the median observed values. For each panel, the total number of data points plotted (N) is given. Note quality control leads to a differing number of data points in each panel.

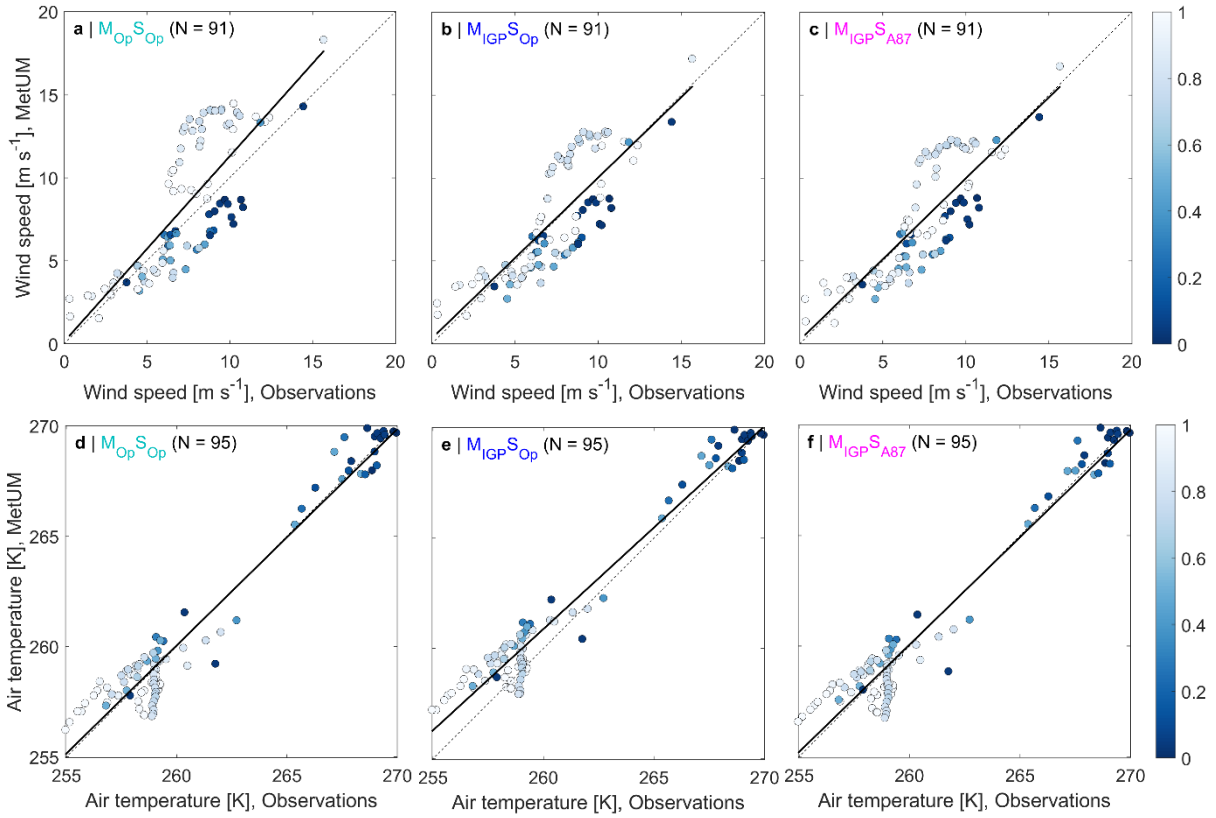

Figure 4 | Scatter plots of observed and modelled (a–c) wind speed and (d–f) air temperature for the IGP data. The shading is ice fraction. The model data are from the MetUM simulations employing the (a, d) $M_{Op}S_{Op}$, (b, e) $M_{IGP}S_{Op}$ and (c, f) $M_{IGP}S_{A87}$ sea ice surface exchange parameterisation configurations. For each panel, the total number of data points plotted (N) is given.

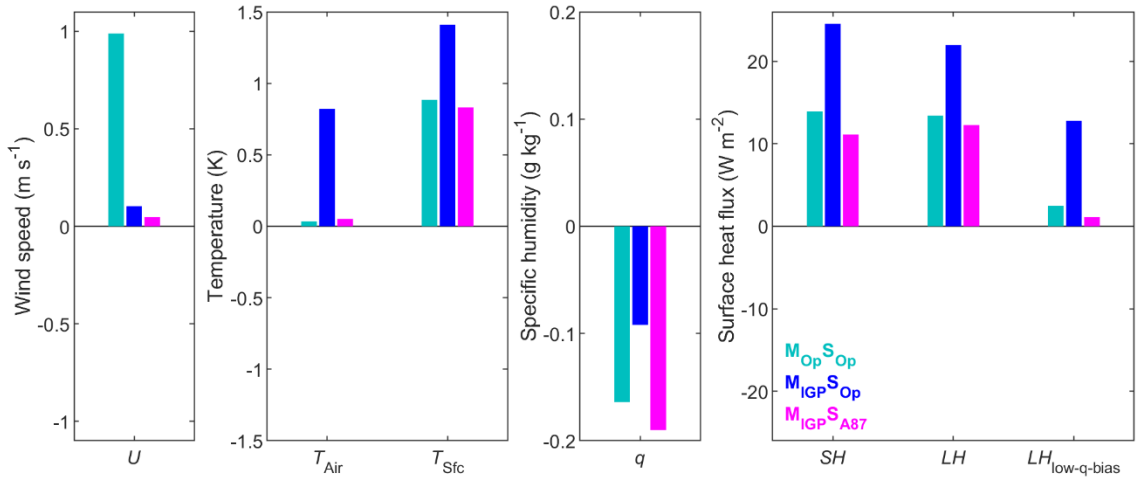

Figure 5 | Model bias relative to IGP aircraft observations in wind speed (U), air and surface temperatures (T_{Air}, T_{Sfc}), specific humidity (q), surface sensible and latent heat fluxes (SH, LH), and LH sub-sampled for when the model bias in q is < 0.1 g kg^{-1} ($LH_{\mathrm{low-q-bias}}$). Biases are shown for the MetUM simulations employing the $M_{Op}S_{Op}$, $M_{IGP}S_{Op}$ and $M_{IGP}S_{A87}$ parameterisation configurations.

		U m s^{-1}	T_{Air} K	T_{Sfc} K	q g kg^{-1}	SH W m^{-2}	LH W m^{-2}	$LH_{\text{low-q bias}}$ W m^{-2}
Mean	Observations	7.4	260.7	263.4	1.24	17	13	18
Standard deviation	Observations	2.9	4.3	5.3	0.51	34	19	19
Model bias	$M_{Op}S_{Op}$	1.0	0.0	0.9	-0.16	14	13	2
	$M_{IGP}S_{Op}$	0.1	0.8	1.4	-0.09	25	22	13
	$M_{IGP}S_{IGP}$	0.0	0.1	0.9	-0.18	12	13	1
	$M_{IGP}S_{A87}$	0.0	0.0	0.8	-0.19	11	12	1
Model RMSE	$M_{Op}S_{Op}$	2.71	1.03	2.35	0.26	34	23	21
	$M_{IGP}S_{Op}$	1.97	1.23	2.61	0.21	44	31	31
	$M_{IGP}S_{IGP}$	1.87	0.98	2.34	0.26	31	23	15
	$M_{IGP}S_{A87}$	1.90	1.05	2.31	0.27	30	22	15

Table 2 | Statistics in key diagnostics for IGP observations and model simulations
Observational mean and standard deviation, plus model bias and root mean square error (RMSE) for the four model experiments. Results are shown for wind speed (U), air and surface temperatures (T_{Air}, T_{Sfc}), specific humidity (q), surface sensible and latent heat fluxes (SH, LH), and LH sub-sampled for when the model bias in q is < 0.1 g kg^{-1} ($LH_{\mathrm{low-q-bias}}$). Note that positive surface heat flux values indicate upward fluxes. For each variable, the lowest bias and RMSE are underlined.

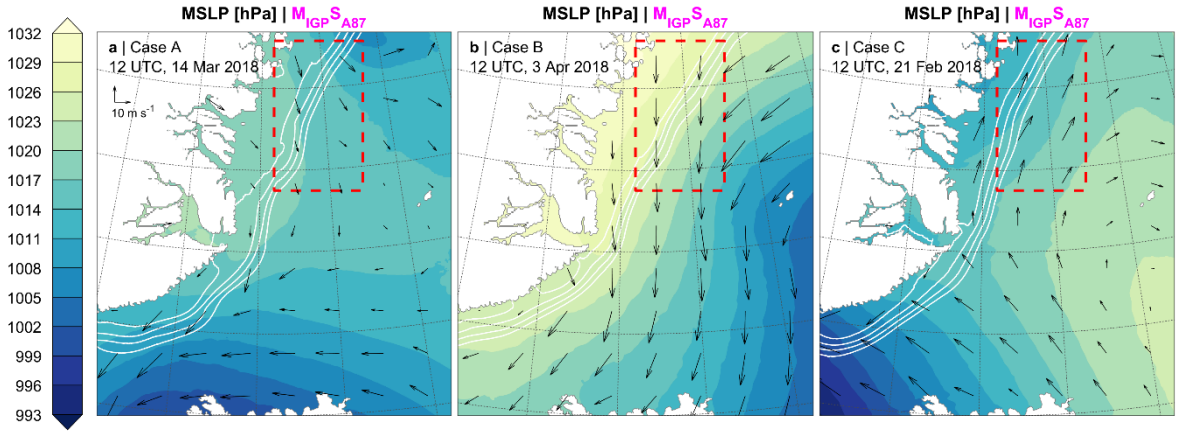

Figure 6 | Maps of mean pressure at sea level (MSLP) and wind vectors at ~100 m altitude over the Iceland and Greenland Seas at representative times (indicated on panels) during (a) Case A, (b) Case B, and (c) Case C, from the MetUM simulations employing the $M_{IGP}S_{A87}$ parameterisation configuration. Reference wind vectors in panel (a) apply to all three panels. White contours show sea-ice concentrations 0.2, 0.4, 0.6, 0.8 and 1. Data is masked over Greenland (top left) and Iceland (bottom). The region enclosed by the dashed red line is used for the statistics presented in Figures 7, 11 and 12.

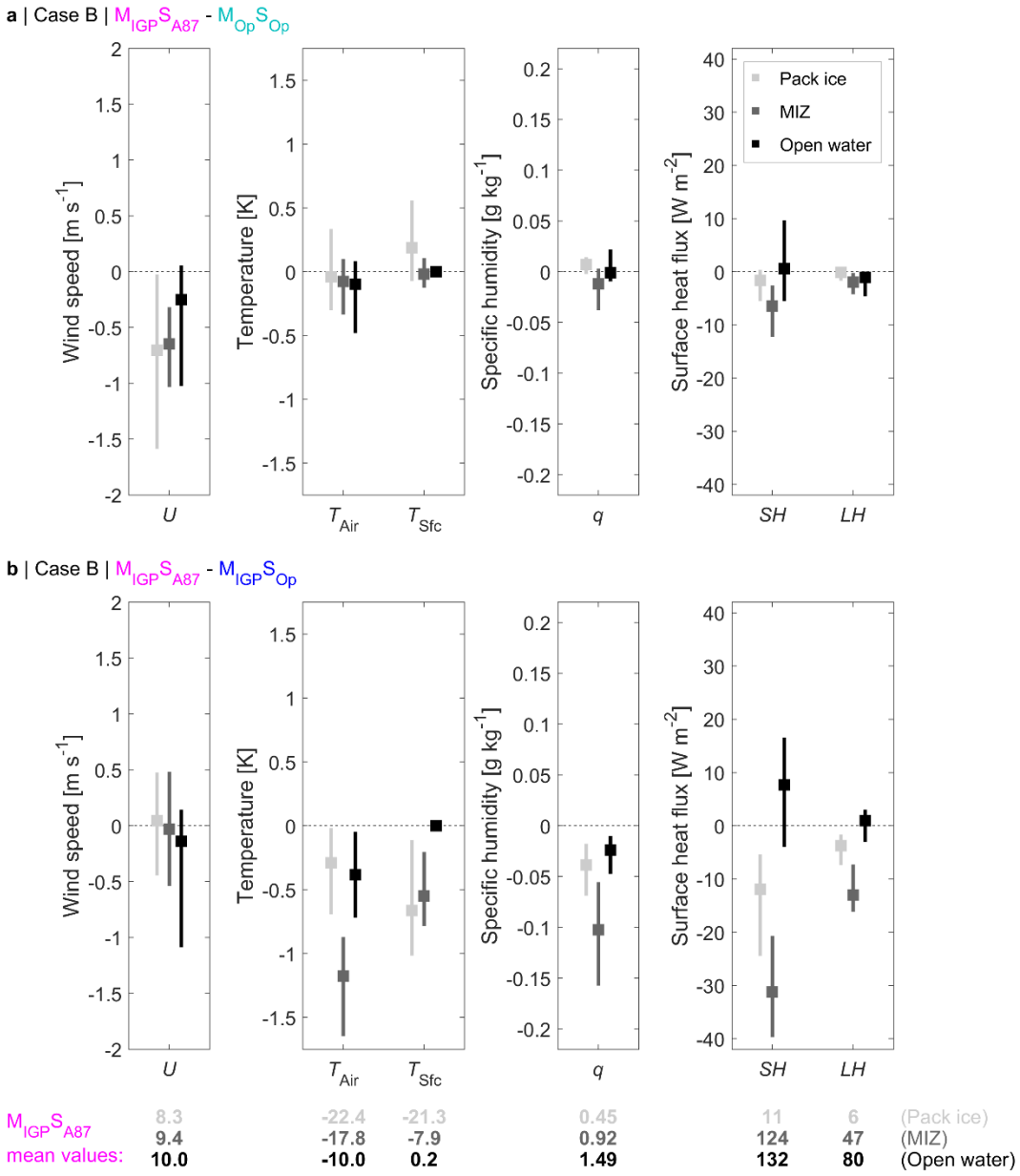

Figure 7 | Summary of differences between (a) the $M_{IGP}S_{A87}$ and $M_{Op}S_{Op}$ simulations and (b) the $M_{IGP}S_{A87}$ and $M_{IGP}S_{Op}$ simulations in key variables over different surfaces during Case B. Panels show the temporal mean (box) and temporal range (whiskers) in the spatial mean differences over consolidated/pack ice (sea-ice concentration > 0.8, light grey), the MIZ (0 < sea-ice concentration ≤ 0.8, dark grey) and open water (sea-ice concentration = 0, black), for the 60-hour duration of Case B within the region enclosed by the red dashed line in Figures 6, 8, 9 and 10. The differences shown are in wind speed (U), air and surface temperatures (T_{Air}, T_{Sfc}), specific humidity (q), surface sensible and latent heat fluxes (SH, LH), and are given as (a) $M_{Op}S_{Op}$ data subtracted from $M_{IGP}S_{A87}$ data and (b) $M_{IGP}S_{Op}$ data subtracted from $M_{IGP}S_{A87}$ data. At the bottom of the figure, mean values from $M_{IGP}S_{A87}$ are given for each variable and surface type.

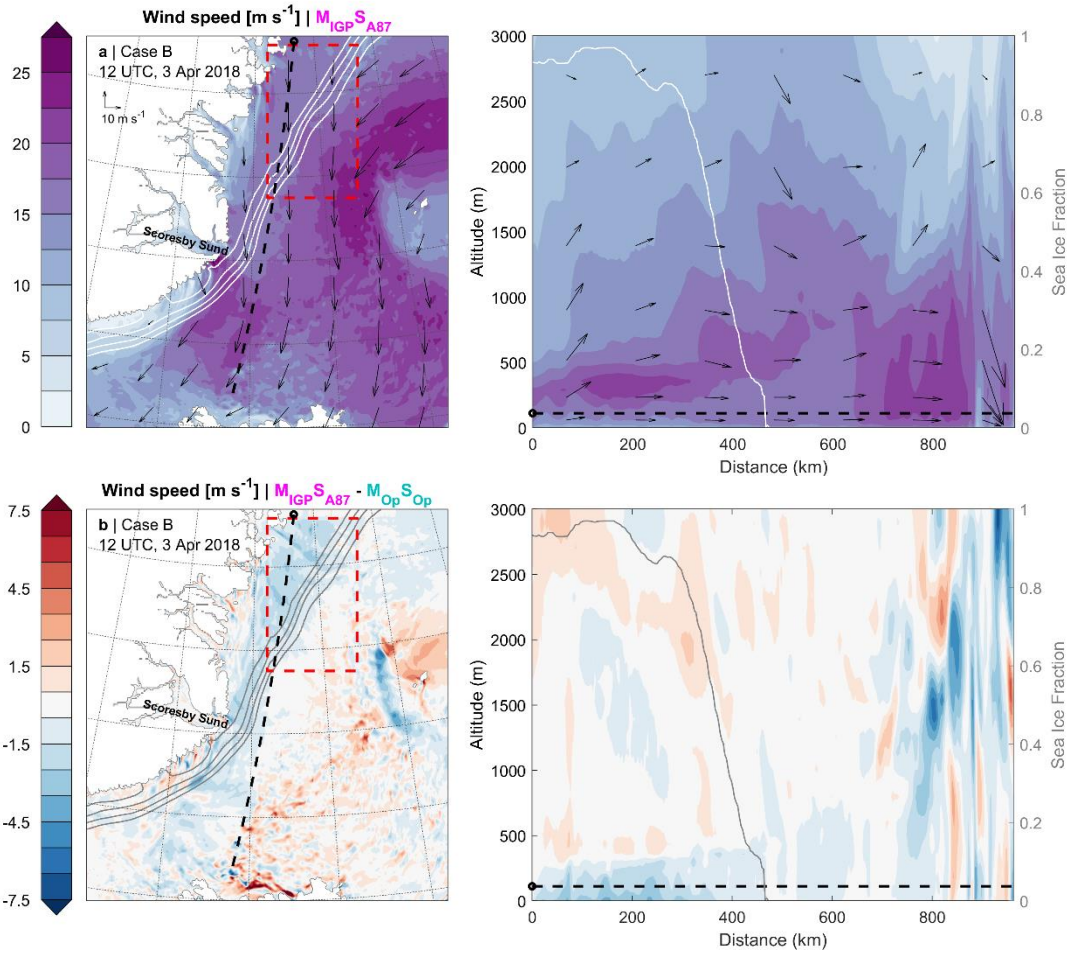

Figure 8 | Maps (left) and cross sections (right) of (a) wind speed and vectors from the $M_{IGP}S_{A87}$ simulation and (b) wind speed difference between the $M_{IGP}S_{A87}$ and $M_{Op}S_{Op}$ simulations ($M_{IGP}S_{A87}$ - $M_{Op}S_{Op}$), over the Iceland and Greenland Seas at 12 UTC on 3 April 2018 during Case B. Sea-ice fraction is shown in the map plots as contours (at 0.2, 0.4, 0.6, 0.8 and 1) in (a) white and (b) grey, and in the cross sections (right axis). The black dashed line in the map plots shows the position of the cross-section, with the circle indicating the start. The black dashed line in the cross sections indicates the height of the wind data used in the map plots (~100 m). The region enclosed by the dashed red line is used for the statistics presented in Figures 7, 11 and 12. In panel (a), reference wind vectors apply to the vectors in the map plot and the horizontal component of the vectors in the cross section; the vertical scale of the vectors in the cross section is in proportion to the horizontal scale, given the cross-section's aspect ratio.

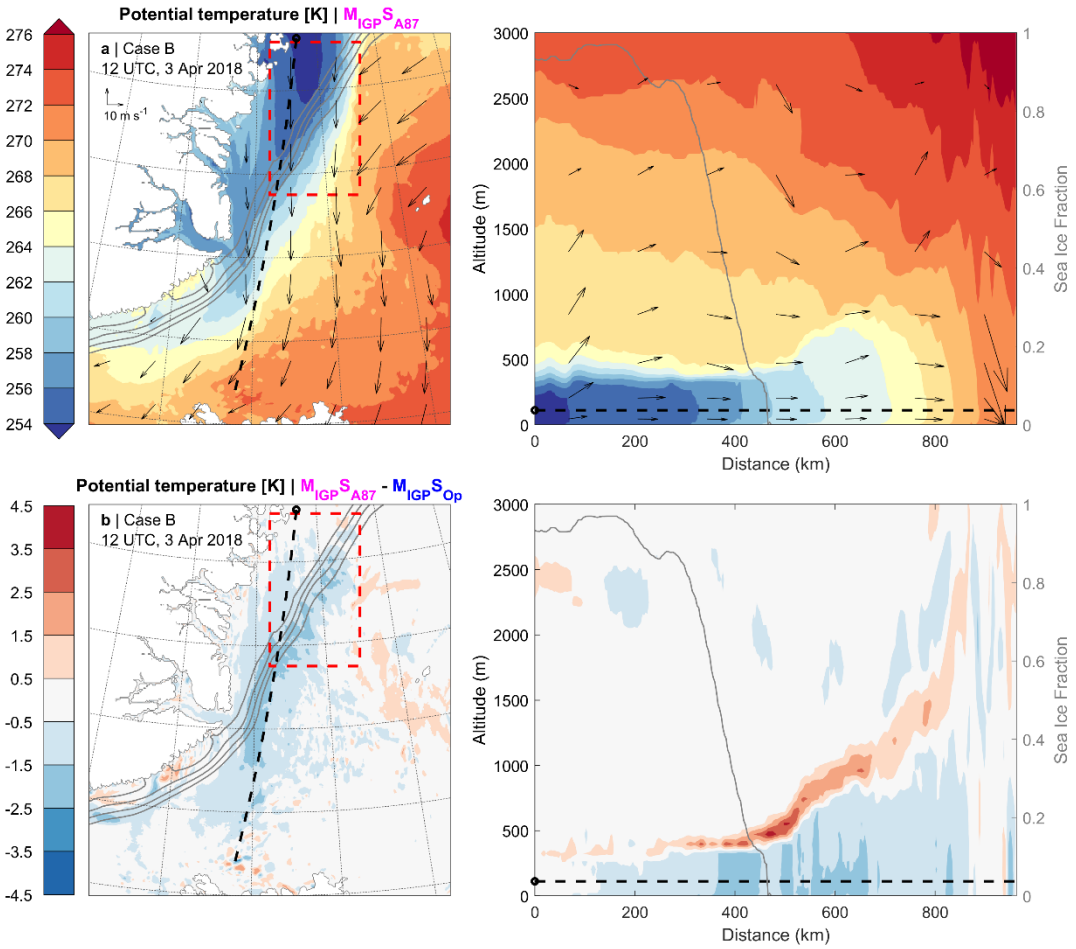

Figure 9 | Maps (left) and cross sections (right), as in Figure 8, but for potential temperature and with the difference plots being for $M_{IGP}S_{A87}$ - $M_{IGP}S_{Op}$ (i.e., the difference due to the scalar parameterization settings).

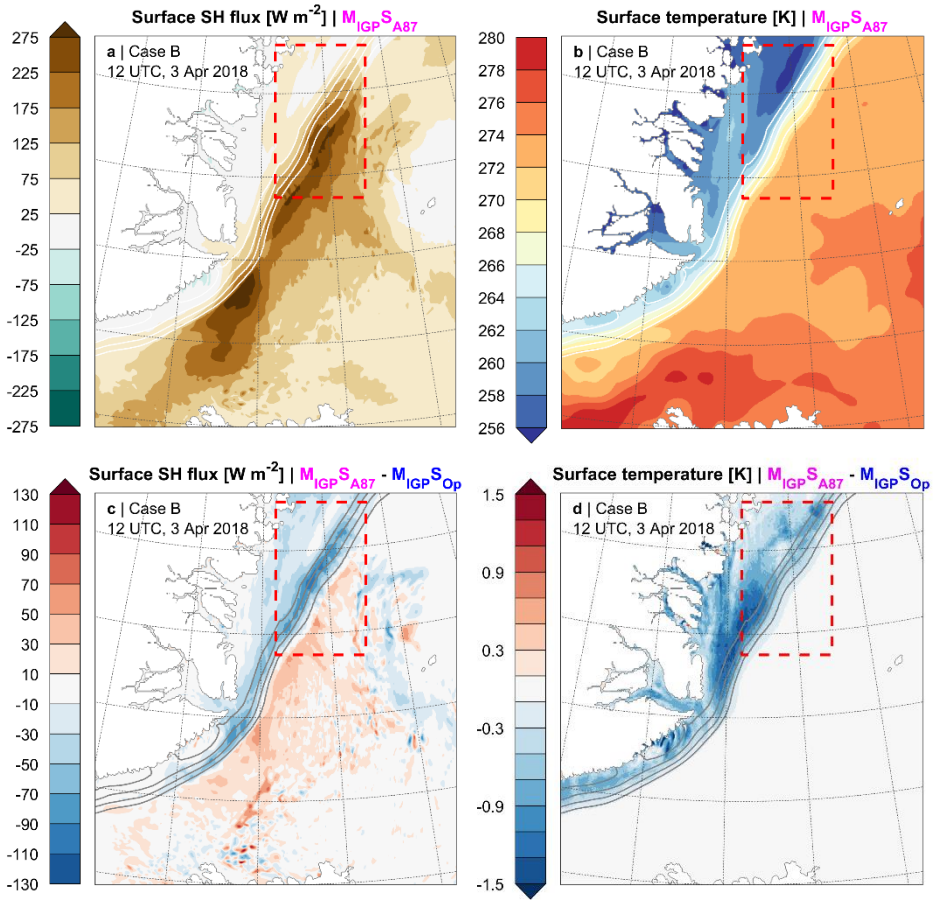

Figure 10 | Maps, as in Figure 9, but for (a, c) surface sensible heat flux and (b, d) surface temperature.

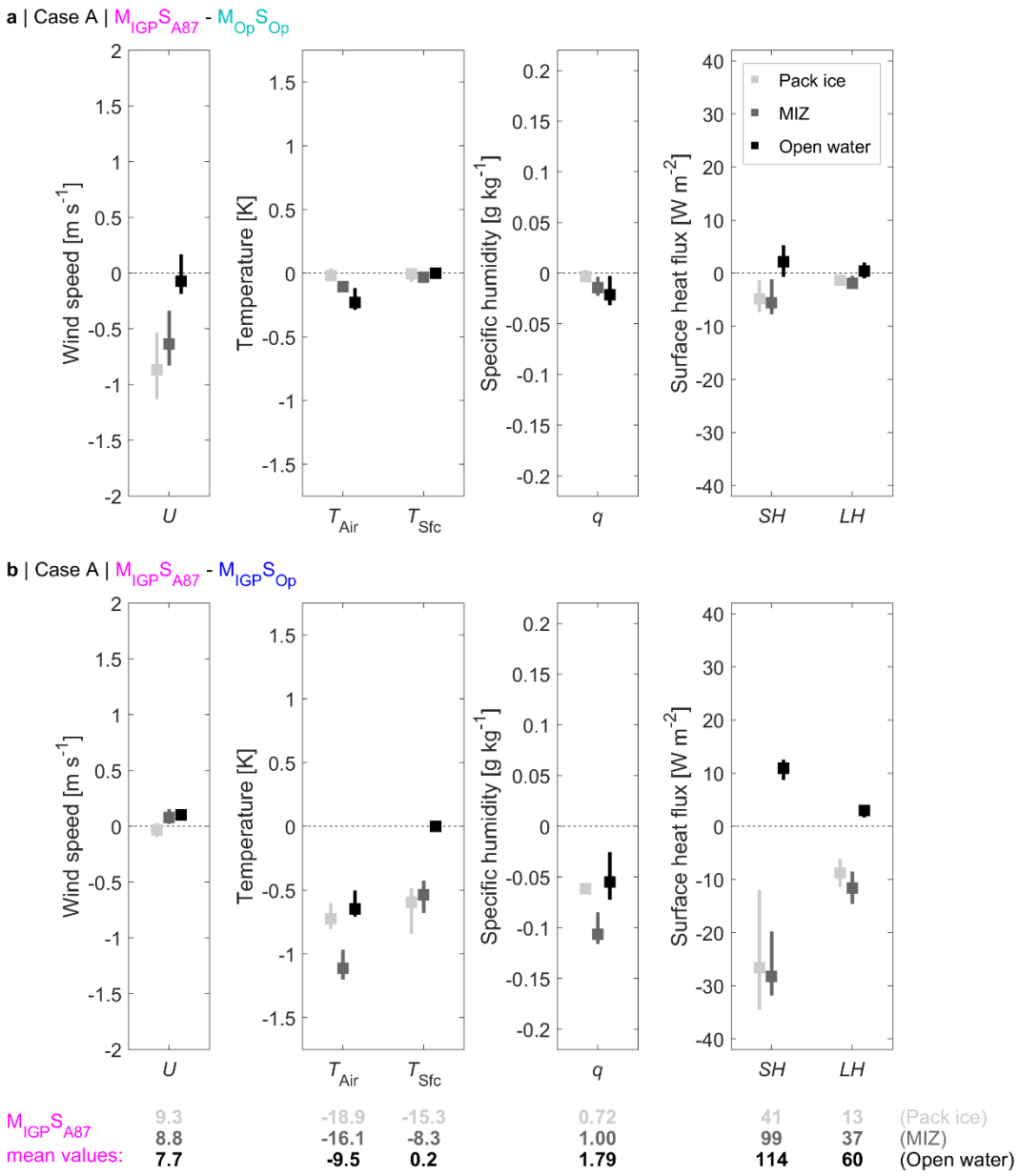

Figure 11 | Summary of differences between (a) the $M_{IGP}S_{A87}$ and $M_{Op}S_{Op}$ simulations and (b) the $M_{IGP}S_{A87}$ and $M_{IGP}S_{Op}$ simulations in key variables, as Figure 7, but during Case A (6 to 18 UTC on 14 March 2018).

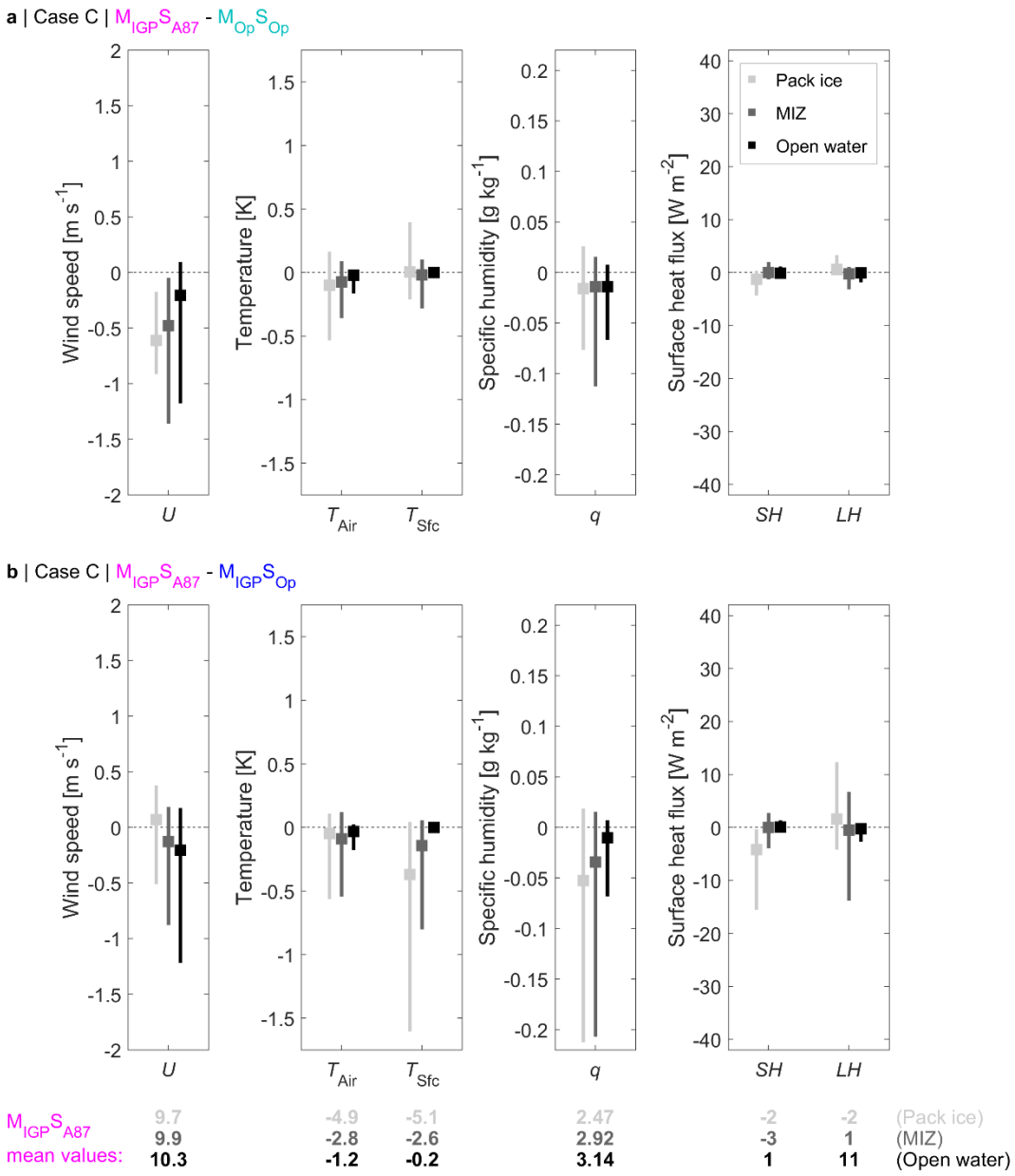

Figure 12 | Summary of differences between (a) the $M_{IGP}S_{A87}$ and $M_{Op}S_{Op}$ simulations and (b) the $M_{IGP}S_{A87}$ and $M_{IGP}S_{Op}$ simulations in key variables, as Figure 7, but during Case C (12 UTC on 17 February 2018 to 0 UTC on 22 February 2018).

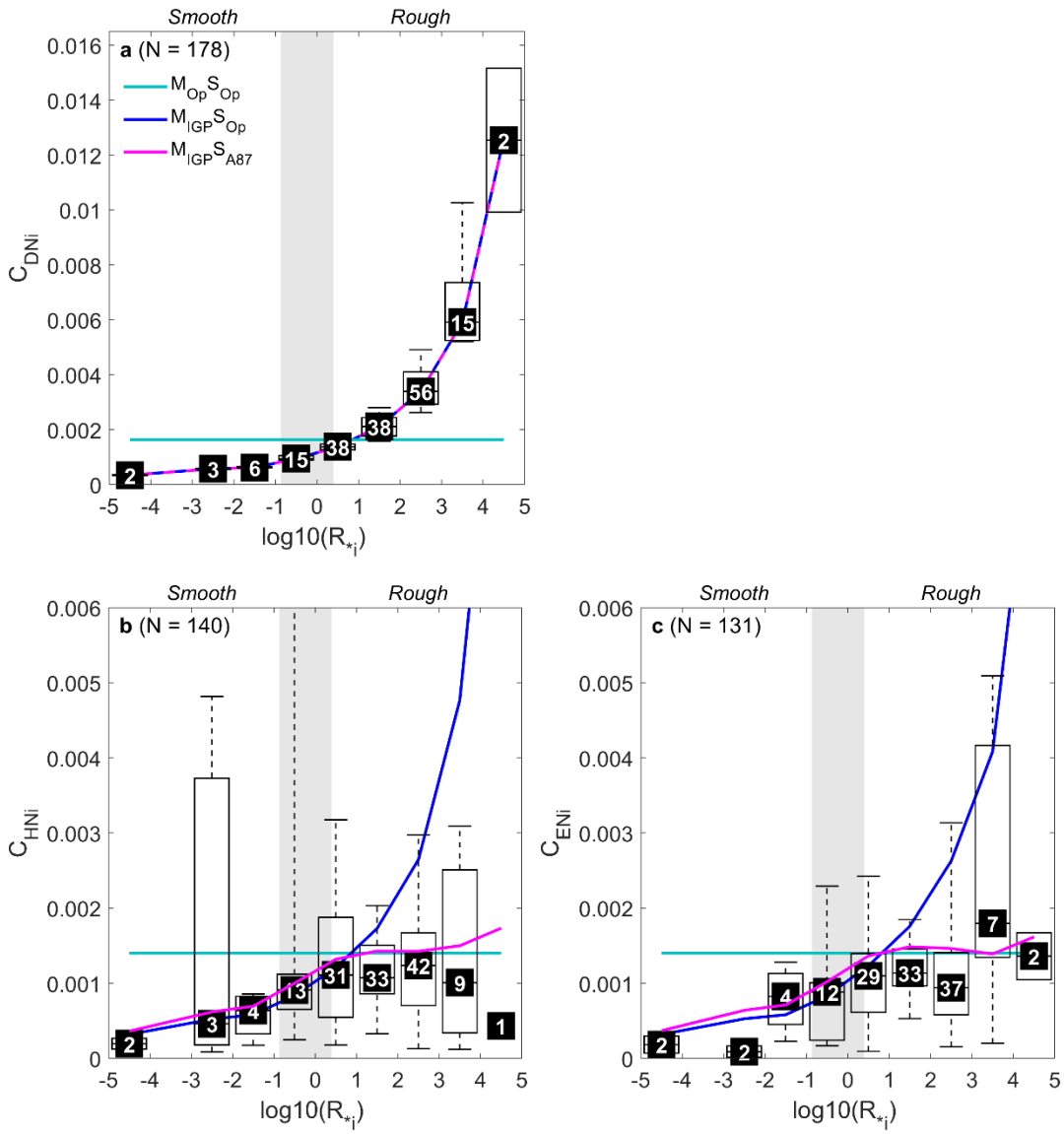

Figure 13 | Surface exchange coefficients for a) momentum, b) heat and c) moisture as functions of R_{*i} (the roughness Reynolds number over sea ice) for the IGP and ACCACIA aircraft observations where sea-ice fraction >0.5, and for the $M_{Op}S_{Op}$, $M_{IGP}S_{Op}$ and $M_{IGP}S_{A87}$ parameterisation schemes. Following Figure 3, panels show observations as box and whiskers plots with the median (horizontal line), interquartile range (open box) and 10th and 90th percentiles (whiskers). The number of data points in each bin is shown at the median value. Gray background shading marks the *transitional* aerodynamic roughness regime, to the left of which ($R_* \leq 0.135$) is the *smooth* regime, and to the right of which ($R_* \geq 2.5$) is the *rough* regime. For each panel, the total number of data points plotted (N) is given.